



## Size-dependence of the heat capacity and thermodynamic properties of hematite ( $\alpha$ -Fe<sub>2</sub>O<sub>3</sub>)

Claine L. Snow, Christopher R. Lee, Quan Shi, Juliana Boerio-Goates, Brian F. Woodfield \*

Department of Chemistry and Biochemistry, Brigham Young University, Provo, UT 84602, USA

### ARTICLE INFO

#### Article history:

Received 9 March 2010

Received in revised form 13 April 2010

Accepted 17 April 2010

Available online 22 April 2010

#### Keywords:

Hematite

Fe<sub>2</sub>O<sub>3</sub>

Nanoparticle

Heat capacity

Magnetism

### ABSTRACT

The heat capacity of a 13 nm hematite ( $\alpha$ -Fe<sub>2</sub>O<sub>3</sub>) sample was measured from  $T = (1.5 \text{ to } 350) \text{ K}$  using a combination of semi-adiabatic and adiabatic calorimetry. The heat capacity was higher than that of the bulk which can be attributed to the presence of water on the surface of the nanoparticles. No anomaly was observed in the heat capacity due to the Morin transition and theoretical fits of the heat capacity below  $T = 15 \text{ K}$  show a small  $T^3$  dependence (due to lattice contributions) with no  $T^{3/2}$  dependence. This suggests that there are no magnetic spin-wave contributions to the heat capacity of 13 nm hematite. The use of a large linear term to fit the heat capacity below  $T = 15 \text{ K}$  is most likely due to superparamagnetic contributions. A small anomaly within the temperature range (4 to 8) K was attributed to the presence of uncompensated surface spins.

© 2010 Elsevier Ltd. All rights reserved.

### 1. Introduction

Hematite ( $\alpha$ -Fe<sub>2</sub>O<sub>3</sub>) is considered to be the most stable form of iron oxide [1], and can be found naturally in rocks, mud, and water systems [1,2]. The catalytic, electronic, and magnetic properties of hematite have been extensively investigated leading to a wide variety of applications. Some technologies that employ hematite include gas sensors, electrode materials in lithium secondary batteries, catalysts, magnetic recording media, and optical and electromagnetic devices as well as water splitting treatments [3–6]. In addition to its many applications, the use of hematite is attractive owing to its non-toxicity, low processing cost, and high resistance to oxidative change [1,2,7].

Studies involving hematite have begun to focus on the size-dependence of its chemical and physical properties [4,5,8,9], and a comparison of bulk and nanoscale behavior reveals significant changes in the properties of hematite. Some studies have concluded that small particle size may alter the energy positions of the electronic states that define the semiconductor band gap [10], yet a recent study suggests no change in the electronic properties of hematite [11]. The magnetic behavior of nanocrystalline hematite has also been shown to deviate from that of bulk hematite. At room temperature bulk hematite is weakly ferromagnetic, but below 260 K ( $T_M$ ) hematite undergoes a first order spin reorientation called the Morin transition [12–15]. The net magnetic

moment is lost in this process, and bulk hematite transforms into an antiferromagnet. In contrast, magnetization studies on nanocrystalline and mesoporous samples of hematite show that no spin reorientation occurs upon cooling [14–21], and ferromagnetic behavior persists as low as  $T = 2 \text{ K}$ . Many studies also show that hematite nanoparticles display superparamagnetic properties [22–24].

In addition to magnetic and electronic measurements, thermodynamic studies of nanosystems provide sophisticated characterization and a more quantitative approach to phase stability [25,26]. A comprehensive thermodynamic study of the many iron oxides and iron oxyhydroxides (FeOOH) has been undertaken by Navrotsky and coworkers [5,27–36] who have recently published a summary of current thermodynamic understanding of these materials [5]. This work has included the measurement of heat capacities and thermochemical measurements which can be used to obtain the standard Gibbs free energy of formation at  $T = 298.15 \text{ K}$ , and bulk hematite has been shown to be the most stable iron oxide with a Gibbs free energy of formation of  $(-744.4 \pm 1.3) \text{ kJ} \cdot \text{mol}^{-1}$ . In these studies, the importance of particle size and degree of hydration has been a key point in determining the energetics of the iron oxide polymorphs [5].

Surface enthalpy (whether comparing wet or dry surfaces) has been shown to be much higher for the anhydrous phases (oxides) than for any of the hydrous phases (oxyhydroxides) [5]. A lower surface enthalpy allows oxyhydroxides to exist with larger surface areas and to be thermodynamically more competitive at smaller particle sizes. This can be seen in the dehydration reaction from goethite ( $\alpha$ -FeOOH) to hematite ( $2\text{FeOOH} = \text{Fe}_2\text{O}_3 + \text{H}_2\text{O}$ ) where

\* Corresponding author. Tel.: +1 801 422 2093; fax: +1 801 422 0153.

E-mail addresses: [brian\\_woodfield@byu.edu](mailto:brian_woodfield@byu.edu), [Brian.Woodfield@chem.byu.edu](mailto:Brian.Woodfield@chem.byu.edu) (B.F. Woodfield).

smaller particle sizes allow goethite to persist to temperatures more than 100 K higher than those calculated by bulk thermodynamic relationships [5]. Another observation of surface enthalpy measurements is that materials with the highest surface enthalpy are stabilized by the adsorption of water [5]. As metastability of the bulk phase increases its surface enthalpy decreases, which has been seen as possibly a close to universal trend and not just with the iron oxides [36]. The decrease of surface enthalpy with increasing metastability of the bulk polymorphs leads to crossovers in free energy of the polymorphs at the nanoscale [5]. This has been seen in the iron oxides as  $\gamma$ -Fe<sub>2</sub>O<sub>3</sub> (maghemite) becomes stable with respect to hematite at the nanoscale, and there are complex crossovers for the FeOOH polymorphs as well [5]. This phenomenon emphasizes the need to consider nanoscale phenomena when studying phase stability and reactivity. In general, the thermodynamics of different polymorphs at the nanoscale depends on the energetics of the bulk polymorphs, the particle size, and the extent of hydration [5].

Size driven thermodynamic differences among iron oxide phases must be taken into account if the formation, stability, and transformation of these materials in geologic, environmental, and industrial settings are to be understood and predicted [5]. Heat capacity measurements of nanocrystalline hematite can aid in this understanding as they can provide information about the density of vibrational states as well as the electronic and magnetic properties of solids [25,26,37,38]. Heat capacities can also be used to generate third-law entropies that, when combined with thermochemical measurements, yield relative free energies of the nanoparticles. In turn, free energies give information about the phase stabilities of the particles relative to each other and to their parent bulk materials.

The heat capacity of bulk hematite was first measured by Parks and Kelley in 1926 over four narrow regions from  $T = (90 \text{ to } 290) \text{ K}$  [39]. In 1958, Westrum and Grønvold [40] improved upon these measurements covering the temperature range from  $(5 \text{ to } 350) \text{ K}$ . No anomaly in the heat capacity due to the Morin transition was observed in this study or in another later series of measurements [41] in 1985 by Jayasuriya *et al.* While Jayasuriya did not provide any values for the entropy of hematite, Westrum and Grønvold calculated the entropy of hematite at  $T = 298.15 \text{ K}$  to be  $87.40 \text{ J} \cdot \text{mol}^{-1} \cdot \text{K}^{-1}$ . Recently, the heat capacity of nanocrystalline hematite was measured within the temperature range  $(253 \text{ to } 283) \text{ K}$  with a reported accuracy of  $\pm 1.5\%$  [42]. Because of its narrow temperature range, these data are insufficient to calculate the entropy associated with nanocrystalline hematite; however, the authors state that their research purpose was to study the magnetocaloric effect in nanosystems, and thus thermodynamic calculations and physical modeling of heat capacity were not within their scope.

While the heat capacity of nanocrystalline hematite has not been adequately measured, heat capacity measurements for several metal and metal oxide nanoparticle systems are available [43–47]. It was previously accepted that the heat capacity of nanoparticles exceeds that of their bulk counterparts with the larger heat capacity being attributed to the increase of surface atoms, which have different vibrational modes than interior atoms [48]. More recently, a careful study regarding the origin of the excess heat capacity in nanoparticles was carried out by Boerio-Goates *et al.* [38] on anatase and rutile polymorphs of TiO<sub>2</sub>. The heat capacity of 7 nm TiO<sub>2</sub> nanoparticles decreased proportionally with the degree of hydration, and the excess heat capacity was shown to be caused by water adsorbed onto the surface of the nanoparticles. When the contributions of the adsorbed water were subtracted from the heat capacity it was shown that, within experimental error, the bare small particle heat capacity was the same as that of the bulk. Also, the water showed two types of behavior. Layers of water closer to the surface of the nanoparticles had a low heat

capacity due to tight binding while outer layers were similar to liquid water. These studies by Boerio-Goates *et al.* agree with the conclusions of Navrotsky *et al.* [5] that the degree of hydration must be taken into account when studying the thermodynamic properties of nanosystems.

This work aims to complement the thermodynamic studies of the iron oxides undertaken by Navrotsky *et al.* Like the measurements carried out on nanocrystalline TiO<sub>2</sub> polymorphs, this study will compare the thermodynamic properties of nanocrystalline hematite to those of the bulk material. This study provides the heat capacity of a hematite powder with an average crystal size of 13 nm over the temperature range  $(1.5 \text{ to } 350) \text{ K}$ . A comparison with new bulk hematite data measured from  $T = (2 \text{ to } 300) \text{ K}$  (to be published separately) is made with a discussion on the effects of water adsorbed onto the surface of nanocrystalline hematite.

## 2. Experimental

Nanocrystalline hematite was prepared through a solid state reaction following the method described by Liu *et al.* [49]. Solid NH<sub>4</sub>HCO<sub>3</sub> was combined with 0.9999 mass fraction pure Fe(NO<sub>3</sub>)<sub>3</sub> · 9H<sub>2</sub>O in a 3:1 Fe<sup>3+</sup>:HCO<sub>3</sub><sup>−</sup> molar ratio. The mixture of the two dry powders turned into a wet slurry which rapidly produced bubbles of CO<sub>2</sub>(g). The mixture was continuously ground (15 to 30) min in an alumina mortar until the evolution of bubbles ceased. A dark brown solid precipitated in this slurry which was dried in air at  $T = 323 \text{ K}$  for 20 h. The solid powder was then rinsed with water using a vacuum filtration flask, transferred to a Pyrex dish, then calcined in air at  $T = 540 \text{ K}$  for 45 min.

The sample was characterized by powder X-ray diffraction (XRD) on a Scintag Diffractometer (Cu K $\alpha$  radiation,  $\lambda = 1.54176 \text{ nm}$ ) at a scanning rate of  $0.1 2\theta \cdot \text{min}^{-1}$  and a power of 15 kW over the range  $25^\circ$  to  $70^\circ$ . The resulting pattern (figure 1) showed the product to be pure hematite in agreement with JCPDS card number 00-001-1053. Using the full peak width at half the maximum intensity and the Scherrer formula, the average crystallite diameter was calculated to be 13 nm.

A sample was prepared for transmission electron microscopy (TEM) by dispersing a small amount of hematite powder in ethanol and grinding with an agate mortar and pestle. The mixture was allowed to rest for 24 h in a glass test tube before drawing off the supernatant. A drop of this suspension was then placed on a copper grid with 3 nm carbon backing and microscopy images were acquired using a Tecnai F30 TEM. Micrographs of the hematite

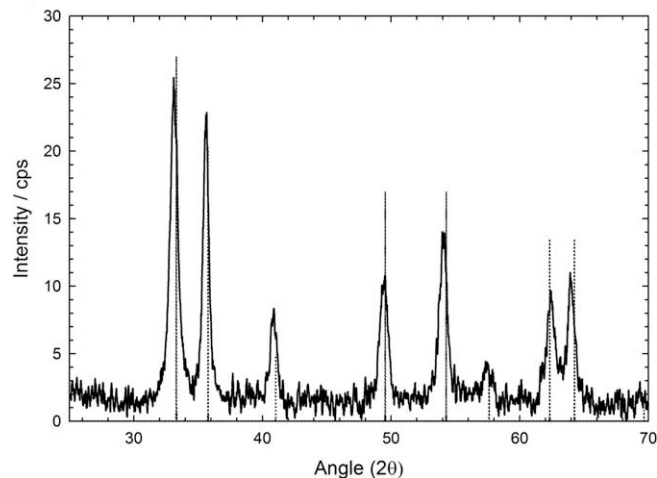


**FIGURE 1.** Powder X-ray diffraction (XRD) spectrum of the 13 nm hematite powder (—) with a comparison to the standard reference pattern (···) found on JCPDS card 00-001-1053.

powder are shown in figures 2a and b. Figure 2a, which shows the particles at 200k $\times$  magnification, gives an idea of the size dispersion and morphology. The particles are roughly spherical, and most have a diameter of  $\sim 10$  nm. Figure 2b shows these particles at 310k $\times$  where ordered atomic planes can be seen, indicating that these particles are highly crystalline in agreement with the results of XRD.

Brunauer Emmett Teller (BET) surface area measurements were performed using a nitrogen adsorption isotherm on a Micromeritics Tristar 3020. The nanohematite powder was found to have a surface area of  $59.0 \text{ m}^2 \cdot \text{g}^{-1}$ . A spherical particle size equivalent can be calculated from surface area measurements using the formula:

$$d \text{ (nm)} = \frac{6}{SA^* \rho} * 1000,$$

where  $\rho$  is the density of the sample. Approximating the density of the nanopowder to be that of bulk hematite ( $5.25 \text{ g} \cdot \text{cm}^{-3}$ ), the particle size is calculated to be 19.4 nm. This formula assumes the

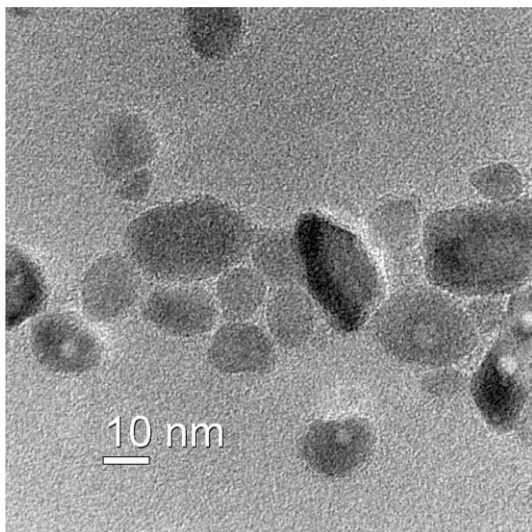


FIGURE 2a. Transmission electron micrograph at 200k $\times$  magnification of the 13 nm hematite powder.

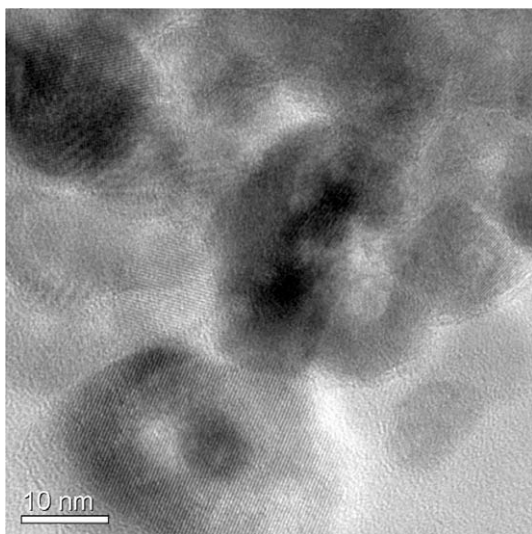


FIGURE 2b. Transmission electron micrograph at 310k $\times$  magnification of the 13 nm hematite powder.

particles to have cubic shape, however if a spherical particle is assumed then this value can be multiplied by the ratio of the surface area of a sphere to that of a cube (0.523) giving a value of 10.1 nm, which is in much better agreement with the results from XRD and TEM.

Analysis of chemical impurities was performed using a Perkin-Elmer inductively coupled plasma optical emission spectrometer (ICP-OES) Optima 4300 DV. A sample solution for ICP was prepared by dissolving two samples (129.0 and 168.6) mg of the hematite powder in  $50.0 \text{ cm}^3$  of 5%  $\text{HNO}_3$ . Qualitative analysis of this sample revealed the presence of Al, Ca, Cr, Mn, and Mg. Quantitative analysis using standard concentrations of these species showed the total impurities to be less than 0.082% of the sample mass making the mass fraction purity of the sample 0.99918 on a metals basis. An analysis of carbon, nitrogen, and hydrogen by combustion at Galbraith Laboratories showed the nitrogen residue from the  $\text{NH}_4\text{HCO}_3$  to be  $68 \cdot 10^{-6}$  while the carbon and hydrogen contents were less than 0.5%.

Thermal gravimetric analysis (TGA) of the sample was carried out in corundum crucibles using a Netzsch 409 system. The sample was heated at a rate of  $8.0 \text{ K} \cdot \text{min}^{-1}$  to  $T = 1273 \text{ K}$  in  $\text{He(g)}$  resulting in a 2.80% mass loss. Assuming all the mass lost to be water, this equates to a per cent mass of hydrogen of 0.313%, which agrees well with the Galbraith results of less than 0.5%. With a detailed characterization, the chemical formula of the hematite nanopowder used in this study is represented as  $\text{Fe}_2\text{O}_3 \cdot 0.248\text{H}_2\text{O}$  with a molar mass of  $164.156 \text{ g} \cdot \text{mol}^{-1}$ .

The sample was prepared for adiabatic calorimetry by compressing the powder into pellets of 9 mm diameter which were then broken and placed in the calorimetric vessel described by Stevens and Boerio-Goates [50]. This container was evacuated and re-filled with 0.080 mmols of dry  $\text{He(g)}$ . The calorimeter was then sealed by pressing a 0.7620 g gold gasket against a stainless steel knife edge located at the top of the vessel. Heat capacity measurements were made on this system over the temperature range (30 to 350) K.

The heat capacity of this sample was also measured within the temperature range (0.5 to 38) K using the semi-adiabatic calorimeter described by Lashley *et al.* [51]. This was done using a 0.1906 g sample wrapped in a 0.0841 g copper foil (mass fraction purity 0.99999) to provide greater thermal conductivity. The copper and hematite nanopowder were compressed into a pellet of 9 mm diameter and 3 mm thickness which was then attached to the sample platform of the apparatus by using Apiezon N grease. The contributions of the copper, grease, and addenda were subtracted to obtain the molar heat capacity of nanocrystalline hematite. The thermometry for both the adiabatic and semi-adiabatic instruments has been calibrated on the ITS-90 temperature scale and the accuracy was generally found to be better than 0.1% for the adiabatic apparatus and 0.5% for the semi-adiabatic apparatus through the measurement of pure copper.

### 3. Results

Experimental results for the molar heat capacity  $C_{p,m}$  of the nanocrystalline hematite powder are given in table 1 along with the temperature increments  $\Delta T$  for each heat capacity measurement. Figure 3 shows the results graphically with a comparison to two bulk data sets measured by PPMS [52] as well as the heat capacity of bulk hematite measured by Westrum and Grønvdal [40]. The heat capacity divided by temperature is shown for the temperature range (1.5 to 10) K in figure 4.

It can be seen in these graphs that, like other nanomaterials, the heat capacity of nanocrystalline hematite is larger than that of the bulk. Also, the spin-flip transition at  $T_M$  is not observed in the heat



Experimental heat capacity of nanocrystalline hematite.  $M = 164.156 \text{ g} \cdot \text{mol}^{-1}$ .

T/K	$C_{p,m}/J \cdot mol^{-1} \cdot K^{-1}$	$\Delta T/K$	T/K	$C_{p,m}/J \cdot mol^{-1} \cdot K^{-1}$	$\Delta T/K$
Series 1			40.15	5.396	3.57
159.13	64.866	2.82	43.91	6.769	3.95
163.08	66.801	5.09	Series 11		
168.18	69.052	5.09	41.99	5.859	3.43
173.28	71.343	5.10	45.62	7.280	3.75
177.7	73.225	3.88	49.61	8.942	4.24
Series 2			54.08	11.135	4.69
192.39	79.228	5.12	59.05	13.386	5.22
197.50	81.318	5.11	Series 12		
202.62	83.259	5.12	1.726	0.002622	0.166
207.75	85.126	5.13	1.897	0.002977	0.185
212.88	86.969	5.13	2.088	0.003394	0.199
218.01	88.857	5.13	2.298	0.003988	0.220
223.14	90.638	5.14	2.528	0.004683	0.240
228.28	92.283	5.14	2.781	0.005564	0.266
Series 3			3.060	0.006745	0.292
219.40	89.20	5.11	3.368	0.008285	0.323
224.52	91.03	5.14	Series 13		
229.65	92.74	5.14	9.157	0.09291	0.875
234.79	94.41	5.14	10.073	0.11885	0.964
239.94	96.09	5.14	11.082	0.15264	1.060
245.08	97.63	5.15	12.191	0.19559	1.164
250.23	99.22	5.15	13.404	0.25298	1.270
255.38	100.68	5.15	14.740	0.32877	1.414
260.53	102.23	5.15	16.222	0.41833	1.559
265.68	103.70	5.16	17.845	0.56851	1.705
270.83	105.12	5.16	19.632	0.75521	1.880
275.99	106.43	5.16	21.601	0.99091	2.065
Series 4			23.761	1.33421	2.266
263.07	102.817	5.40	26.119	1.77470	2.464
268.34	104.287	5.15	28.712	2.34062	2.738
273.50	105.659	5.16	31.578	3.10029	3.010
278.66	106.883	5.17	34.730	4.09817	3.311
283.82	108.345	5.15	37.552	4.93222	2.352
288.97	109.750	5.16	Series 14		
294.14	111.168	5.17	1.812	0.002819	0.173
299.30	112.446	5.16	1.992	0.003221	0.190
304.46	113.746	5.17	2.193	0.003749	0.207
309.62	115.080	5.17	2.411	0.004362	0.231
314.78	116.255	5.18	2.654	0.004985	0.251
319.95	117.371	5.17	2.923	0.006086	0.280
Series 5			3.212	0.007206	0.307
296.58	111.778	5.25	3.534	0.009041	0.336
301.78	112.954	5.16	3.887	0.010769	0.366
306.94	114.080	5.17	4.275	0.013272	0.407
312.11	115.455	5.16	4.701	0.017728	0.448
Series 6			5.170	0.022685	0.491
317.23	116.357	5.11	5.684	0.029664	0.543
322.37	117.499	5.17	6.258	0.037346	0.594
327.54	118.725	5.17	6.883	0.046173	0.657
332.71	119.710	5.17	7.570	0.056935	0.717
337.88	120.881	5.17	8.327	0.070361	0.790
343.05	121.706	5.17	9.152	0.091213	0.871
348.23	122.697	5.17	10.066	0.115613	0.962
353.41	123.683	5.17	Series 15		
Series 7			9.618	0.1051	0.921
60.08	13.824	9.50	10.580	0.1347	1.005
67.01	17.274	4.35	11.637	0.1732	1.110
71.54	19.555	4.72	12.795	0.2251	1.206
76.28	22.039	4.75	14.068	0.2892	1.342
81.05	24.610	4.79	15.477	0.3777	1.481
85.87	27.239	4.83	17.032	0.4961	1.631
90.72	29.910	4.87	18.741	0.6542	1.792
95.61	32.646	4.90	20.622	0.8588	1.972
100.53	35.339	4.93	22.684	1.1514	2.164
105.47	38.038	4.95	24.942	1.5389	2.367
110.43	40.766	4.97	27.419	2.0477	2.601
115.41	43.479	4.99	30.145	2.6922	2.858
Series 8			33.149	3.5614	3.172
97.87	33.802	4.39	36.140	4.5749	2.842
102.54	36.431	4.95	Series 16		
107.49	39.181	4.96	1.347	0.001791	0.127
112.46	41.860	4.98	1.482	0.002085	0.141
117.45	44.531	5.00	1.628	0.002422	0.157

---

$T/K$	$C_{p,m}/J \cdot mol^{-1} \cdot K^{-1}$	$\Delta T/K$	$T/K$	$C_{p,m}/J \cdot mol^{-1} \cdot K^{-1}$	$\Delta T/K$
122.46	47.181	5.01	1.792	0.002754	0.175
127.47	49.832	5.02	1.972	0.003172	0.189
132.50	52.410	5.04	2.169	0.003644	0.208
137.55	54.939	5.05	Series 17		
142.60	57.439	5.06	1.418	0.001945	0.139
147.66	59.898	5.06	1.558	0.002264	0.143
152.73	62.287	5.08	1.711	0.002560	0.165
Series 9			1.883	0.002921	0.179
157.82	64.487	5.03	2.070	0.003370	0.197
162.88	66.732	5.09	Series 18		
167.97	69.077	5.09	3.700	0.009972	0.362
173.07	71.383	5.10	4.075	0.012323	0.386
178.17	73.645	5.11	4.480	0.015204	0.427
183.28	75.730	5.11	4.928	0.019739	0.468
188.39	77.781	5.12	5.419	0.025729	0.517
193.51	79.806	5.12	5.960	0.032922	0.566
198.63	81.777	5.12	6.556	0.041086	0.626
203.75	83.657	5.13	7.211	0.051480	0.683
208.88	85.606	5.13	7.928	0.063731	0.755
214.01	87.424	5.13	8.721	0.081892	0.834
Series 10			9.592	0.10372	0.917
31.01	2.566	2.41	10.552	0.13197	1.010
36.77	4.261	3.19			

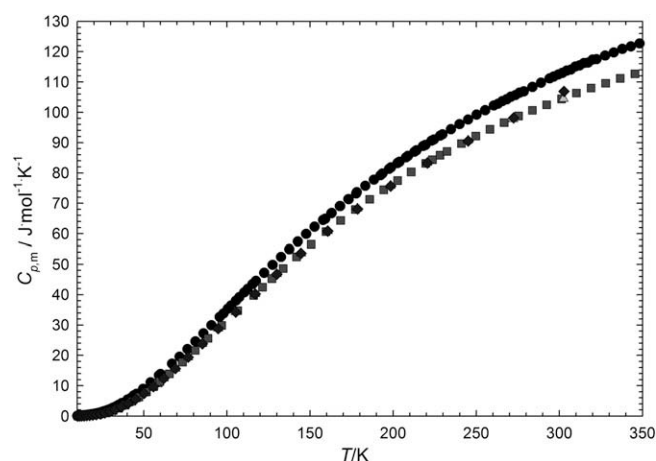


**FIGURE 3.** Plot of heat capacity of 13 nm hematite against temperature (●) with a comparison to the bulk heat capacity measured by Westrum and Grønvdal (■) [40], PPMS Series 1 (▲), and PPMS Series 2 (◆).

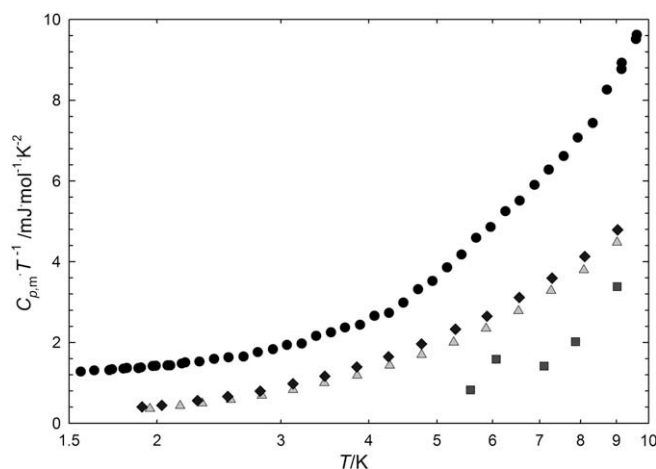


**FIGURE 4.** Plot of  $C_{p,m}/T$  against temperature of 13 nm hematite against temperature (●) shown on a log scale below 10 K with a comparison to the bulk heat capacity measured by Westrum and Grönvold (■) [40], PPMS Series 1 (▲), and PPMS Series 2 (◆).

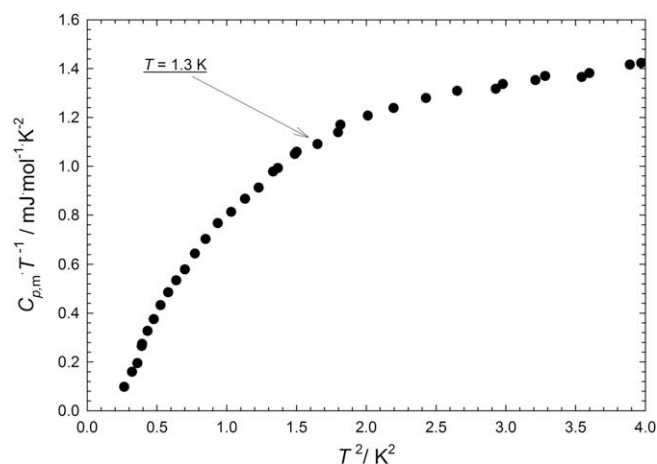


FIGURE 5. Plots of  $C_{p,m}/T$  against  $T^2$  which shows a trend in the data where the heat capacity begins to drop toward negative values at  $T^2 = 1.8$  ( $T = 1.3$  K).

capacity of nanocrystalline hematite. However, no anomaly was observed in the heat capacity of bulk hematite as well [40,41,52]. Another feature from the data is seen within the temperature region from (4 to 7) K where there is a small, broad anomaly. A discussion of the physical implications of the features observed in the heat capacity of nanocrystalline hematite is given below.

The heat capacity was experimentally measured at a temperature as low as 0.5 K, but an examination of the data by plotting  $C/T$  vs.  $T^2$  (figure 5) shows an inflection at  $T = 1.3$  K at which point the data began to trend towards negative values. Attempts to fit the heat capacity of nanocrystalline hematite including these points resulted in large degrees of error, and it was determined that data below  $T = 1.3$  K did not achieve thermal equilibrium during the measurement process.

## 4. Discussion

### 4.1. The Morin transition

The absence of an anomaly in the region of the Morin transition is not surprising since the transition was not observed in the heat capacity of bulk hematite [40,41]. Various studies have placed the temperature of the Morin transition where the sample changes from ferromagnetic to antiferromagnetic at  $T = 250$  K. It has been suggested that the heat capacity shows no sign of transition in this region because either it does not involve any appreciable entropy increment or that it is spread out over a rather broad temperature range [40]. Although the Morin transition has not shown a significant contribution to the heat capacity of hematite, low-temperature fits can help determine whether a magnetic transition has occurred. The following discussion is an analysis of the physical properties of 13 nm hematite that are extracted from low-temperature theoretical fits.

### 4.2. Thermophysical properties of nanocrystalline hematite

Modeling heat capacity data with theoretical functions at low temperatures (<15 K) can provide valuable information about the magnetic, electronic, and vibrational properties of a sample [25]. The total heat capacity can be viewed as a sum of the energetic contributions from the various physical properties of a material. At temperatures above 10 K, the largest contribution to heat capacity stems from lattice vibrations which are modeled by an odd-powers fit [37] to the equation:

$$C_{Lat} = \sum_{n=3,5,7,\dots} B_n T^n. \quad (1)$$

Magnetic contributions will also have a temperature-dependence with  $T^{3/2}$  for ordered ferro- and ferrimagnets and  $T^3$  for antiferromagnets [25]. If there is a significant amount of anisotropy the spin-wave spectrum will have a gap [33,53], which is similar to the gap induced by a magnetic field. Gaps in magnetic solids require the use of the term  $C_{fsw} = B_{fsw} T^{3/2} \exp(-\Delta/T)$  for ferro- and ferrimagnets and  $C_{asw} = B_{asw} T^3 \exp(-\Delta/T)$  for antiferromagnets, where  $\Delta$  is the gap parameter given in units of K. Fits are made by combining some of these models, and a physically meaningful expression that represents the heat capacity of nanocrystalline hematite can be obtained.

Conduction electrons contribute to the heat capacity in a linear fashion with  $\gamma T$  representing the electronic heat capacity in most cases [25]. In addition to conducting solids, a linear term is generally observed in many oxide materials that are not fully stoichiometric or which contain oxygen vacancies or dislocations. For example, non-conducting oxides requiring a linear term include  $\alpha$ -FeOOH (goethite) [33], crystalline pure SiO<sub>2</sub> zeolites [54], and hydrous potassium aluminosilicate (muscovite) [55] where the linear term has been attributed by Coey *et al.* [55] to localized electronic states associated with oxygen vacancies.

Superparamagnetic effects can also contribute to the heat capacity [56,57]. Super-paramagnetism [56–58] occurs in nanoparticles that consist of a single magnetic domain with a diameter between (3 and 50) nm. Unlike the effects of paramagnetism, which are usually observed above the Curie temperature, super-paramagnetism occurs below this point. This magnetic behavior is characterized by the entire nanoparticle acting as a single magnetic moment which can randomly flip direction under the influence of temperature. Super-paramagnetism can be manifest as a dipolar contribution to the heat capacity due to the interaction of each spin cluster with the dipolar field created by all the other neighbors. This dipolar field depends on the spin configuration of the neighboring spins, which is dependent on the overall magnetization, and in the absence of a magnetic field the probability distribution of the internal fields is centered at zero. The heat capacity of ideal superparamagnets frequently exhibits an upturn in the heat capacity at temperatures lower than 1 K as shown in reports by Triplett and Phillips [59]. Livingston and Bean [57] proposed that superparamagnetic effects might make a measurable contribution to  $\gamma$  under optimal conditions which include small particle size and positive anisotropy energy. This model is limited by its neglect of interactions between particles, yet a linear term has been observed in other superparamagnetic systems [59].

### 4.3. Fits of the heat capacity of 13 nm hematite

The presence of a small anomaly in the heat capacity ranging from  $T = (4$  to  $7)$  K presented some difficulties in modeling the thermophysical behavior of nanocrystalline hematite. Attempts to model this data with a Schottky (2-level system) or a magnetic spin gap produced physically meaningless results with parameters having negative values. The points in the region of the anomaly were omitted in subsequent fits, which were done for the range (1.4 to 15) K. This approach was successful, and the heat capacity of nanocrystalline hematite is expressed as:

$$C_{p,m} = \gamma T + B_3 T^3 + B_5 T^5. \quad (2)$$

Table 2 contains the parameters for this expression (fit-1) as well as those for other fits of the heat capacity of nanocrystalline hematite. An inspection of this table shows that fits 2 and 3 do not accurately represent the heat capacity of 13 nm hematite as seen by their high %RMS values. Fits 1 and 4 have a similar %RMS, but fit-4 has a small

TABLE 2

A summary of fits of the low-temperature heat capacity of 13 nm hematite.

Parameter	Fit-1	Fit-2	Fit-3	Fit-4
$B_3/(\text{mJ} \cdot \text{mol}^{-1} \cdot \text{K}^{-4})$	0.098187	0.087202	0.070020	0.10080
$B_5/(\text{mJ} \cdot \text{mol}^{-1} \cdot \text{K}^{-6})$	−5.9318E−05		4.3157E−05	−6.9112E−05
$\gamma/(\text{mJ} \cdot \text{mol}^{-1} \cdot \text{K}^{-2})$	1.0235	0.82085		1.1129
$B_{\text{fsw}}/(\text{mJ} \cdot \text{mol}^{-1} \cdot \text{K}^{-5/2})$		0.17695	0.79806	−0.070675
%RMS	1.47	2.35	4.84	1.42

negative value for  $B_{\text{fsw}}$ . A negative parameter is physically meaningless, but this value is small enough that the spin-wave contribution can be approximated to be zero. Consequently, fit-4 is the same expression as that of fit-1, which suggests that fit-1 gives the most accurate representation of the heat capacity of 13 nm hematite. Support for this conclusion can also be seen in the deviation of the various fits (figure 6) which shows that only fit-1 has a random distribution about zero in the given temperature range. Also, the low-temperature heat capacity of nanocrystalline hematite is compared with fit-1 in figure 7 where it can be seen that this fit agrees well with experimental measurements except in the region of the anomaly from  $T = (4 \text{ to } 8) \text{ K}$ .

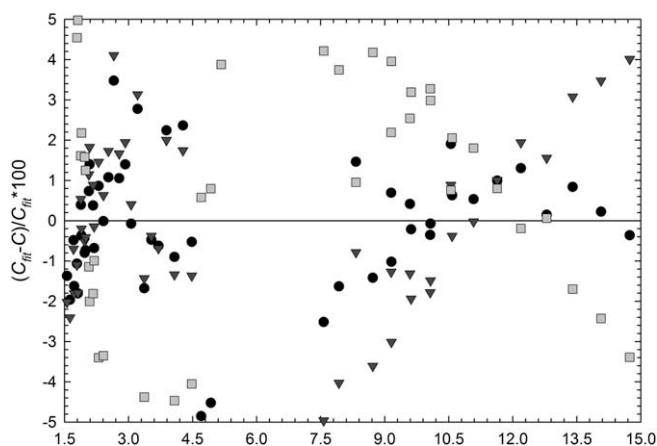


FIGURE 6. Plot of the deviation of fits 1 to 3 from the low-temperature experimental heat capacity of 13 nm hematite against temperature. Fit-1 is represented by circles (●), fit-2 by inverted triangles (▼), and fit-3 by squares (■).

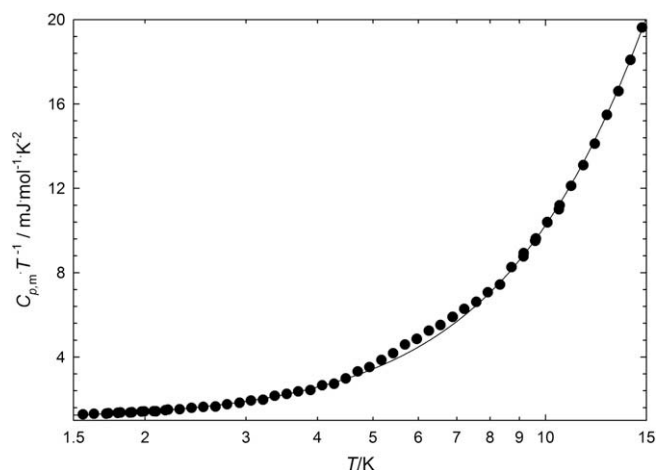


FIGURE 7. Plot of  $C_{p,m}/T$  against temperature to illustrate the low-temperature heat capacity of 13 nm hematite shown on a log scale. The solid line represents a fit of the lattice.

#### 4.4. Physical meaning of fit-1

Fit-1 included terms for the lattice heat capacity and a linear contribution, but no term for a ferromagnetic spin wave is required. This is surprising since several studies indicated that nanocrystalline hematite did not undergo the spin-flip transition to antiferromagnetic behavior, but that it retained ferromagnetic behavior as low as  $T = 2 \text{ K}$ . One possible explanation for this observation is that the sample has transformed to antiferromagnetic which would be manifest in the use of a  $T^3$  term. A second explanation is that the ferromagnetic spin-wave contribution is so small that it does not make a significant difference in the fitting expression, yet this is unlikely since fits 2 and 3 show that  $B_{\text{fsw}}$  can be large but not accurately represent the heat capacity data. Another possibility is that 13 nm hematite does not order magnetically at low temperatures. An analysis of the  $T^3$  contribution is necessary in order to determine whether there is antiferromagnetic ordering in 13 nm hematite.

#### 4.5. Analysis of the $T^3$ dependence

Generally, antiferromagnetic contributions are 10 to 20 times larger than the lattice component at low-temperatures [25]. This can be seen in a comparison of the low-temperature heat capacity of antiferromagnetic  $\text{MnCO}_3$  and nonmagnetic  $\text{CaCO}_3$  [25]. These two samples have a similar lattice contribution but the contribution of  $T^3$  in  $\text{MnCO}_3$  is many times that of  $\text{CaCO}_3$ . In the case of 13 nm hematite, other iron oxides make good candidates for such a comparison. Table 3 shows a list of iron oxides that have been fit at low-temperatures with their respective lattice components and magnetic behavior. It can be seen that 13 nm hematite has a similar lattice contribution to those of bulk hematite and goethite ( $\alpha\text{-FeOOH}$ ) [33]. Bulk hematite was also shown to have a ferromagnetic spin wave while goethite had an anisotropic antiferromagnetic contribution. The similarity and small size of these lattice components suggests that the  $T^3$  dependence in 13 nm hematite stems from the lattice heat capacity with no antiferromagnetic spin wave. This can also be seen in the much larger lattice contribution of 13 nm magnetite ( $\text{Fe}_3\text{O}_4$ ) which had no antiferromagnetic spin-wave component. This conclusion implies that 13 nm hematite has no significant contribution from antiferromagnetic or ferromagnetic ordering.

#### 4.6. Analysis of the linear term

The most common use of a linear term is to represent an electronic contribution [25], yet nanocrystalline hematite is a semiconductor with a band gap of 2.2 eV [11]. As mentioned previously a linear term has been seen for non-conducting oxides that had oxygen vacancies. This phenomenon was observed in the low-temperature heat capacity of goethite [33], which has a similar band gap of 2.5 eV [10]. As seen in table 4, nanocrystalline hematite has a value of  $1.02 \text{ mJ} \cdot \text{mol}^{-1} \cdot \text{K}^{-2}$  for  $\gamma$ , which is significantly larger than the linear contribution for the iron oxyhydroxides [33,60]. The significant difference in these values suggests that the linear term in

**TABLE 3**

A comparison of some fit parameters of various iron oxides. Information for goethite was taken from Majzlan et al. [33] while 13 nm magnetite, lepidocrocite, akaganéite, and bulk hematite are unpublished work from our laboratory [52,60].

Sample	$\gamma/(\text{mJ} \cdot \text{mol}^{-1} \cdot \text{K}^{-2})$	$B_3/(\text{mJ} \cdot \text{mol}^{-1} \cdot \text{K}^{-4})$	$B_{\text{fsw}}/(\text{mJ} \cdot \text{mol}^{-1} \cdot \text{K}^{-5/2})$	$B_{\text{asw}}/(\text{mJ} \cdot \text{mol}^{-1} \cdot \text{K}^{-4})$	Magnetic term
13 nm Hematite	1.02	0.098			None
Bulk hematite		0.083	0.04		Ferromagnetic
37 nm Goethite ( $\alpha$ -FeOOH)	0.23	0.1		1.2	Anisotropic antiferromagnetic
13 nm Magnetite ( $\text{Fe}_3\text{O}_4$ )	3.46	0.59	75.8		Anisotropic ferrimagnetic
30 nm Lepidocrocite ( $\gamma$ -FeOOH)	0.35	0.496		9.65	Anisotropic antiferromagnetic
34 nm Akaganéite ( $\beta$ -FeOOH)	0.47	0.218		0.514	Anisotropic antiferromagnetic

**TABLE 4**

A comparison of the surface hydration of nanoparticulate rutile and anatase polymorphs with that of nanocrystalline hematite. Values for  $\text{TiO}_2$  polymorphs were taken from Boerio-Goates et al. [38] except  $\text{H}_2\text{O} \cdot \text{nm}^{-2}$  which were calculated from the other values.

	$\text{TiO}_2$ anatase “outer water”	$\text{TiO}_2$ anatase “inner water”	$\text{TiO}_2$ rutile “outer water”	$\text{TiO}_2$ rutile “inner water”	13 nm Hematite
SA (BET)/( $\text{m}^2 \cdot \text{g}^{-1}$ )	250	250	104	104	56.1
Moles $\text{H}_2\text{O}$ per mole sample	0.677	0.379	0.361	0.244	0.248
$M/(\text{g} \cdot \text{mol}^{-1})$	92.062	86.694	86.369	84.262	164.156
$\text{H}_2\text{O} \cdot \text{nm}^{-2}$	17.7	10.5	24.2	16.8	16.2

fit-1 does not originate from localized electronic states associated with oxygen vacancies.

Magnetic studies of hematite nanoparticles at low-temperatures have shown superparamagnetic behavior [22–24], and it is likely that the linear term stems from a superparamagnetic contribution. To the best of our knowledge, no heat capacity studies have been performed by any other groups on superparamagnetic nanosystems. Triplett and Phillips [59] reported a  $\gamma$  value of  $13.3 \text{ mJ} \cdot \text{mol}^{-1} \cdot \text{K}^{-2}$  for the bulk compound  $\text{Ni}_{0.62}\text{Rh}_{0.38}$ , which was shown to have anomalous behavior consistent with superparamagnetic clusters. However in this study, no mention was made of the relationship of the linear term with superparamagnetic behavior, although Livingston and Bean [57] had already suggested such a relationship. Instead it was assumed that all of the linear term was due to the electronic specific heat as  $\text{Ni}_{0.62}\text{Rh}_{0.38}$  was a conducting solid. The electronic contribution to the heat capacity of Ni metal [25] is  $7.28 \text{ mJ} \cdot \text{mol}^{-1} \cdot \text{K}^{-2}$  while Rh metal [25] has value of  $4.89 \text{ mJ} \cdot \text{mol}^{-1} \cdot \text{K}^{-2}$ . By multiplying the value of Ni by 0.62 and that of Rh by 0.38 then adding them together, the electronic contribution to the heat capacity of  $\text{Ni}_{0.62}\text{Rh}_{0.38}$  can be estimated to be  $6.37 \text{ mJ} \cdot \text{mol}^{-1} \cdot \text{K}^{-2}$ . This value is well below  $13.3 \text{ mJ} \cdot \text{mol}^{-1} \cdot \text{K}^{-2}$  as reported by Triplett and Phillips, and it is possible that the linear contribution in their study had a superparamagnetic component. Estimates of the linear term like that made for  $\text{Ni}_{0.62}\text{Rh}_{0.38}$  are more accurate for conducting alloys that are not superparamagnetic. This can be seen in CuZn [61] which has a linear contribution of  $0.69 \text{ mJ} \cdot \text{mol}^{-1} \cdot \text{K}^{-2}$  while our method of estimating the linear term predicts a value of  $0.66 \text{ mJ} \cdot \text{mol}^{-1} \cdot \text{K}^{-2}$  [25]. Likewise,  $\text{Ni}_{0.47}\text{Cu}_{0.53}$  [62] had a value of  $3.10 \text{ mJ} \cdot \text{mol}^{-1} \cdot \text{K}^{-2}$  while our estimate was  $3.20 \text{ mJ} \cdot \text{mol}^{-1} \cdot \text{K}^{-2}$  [25]. Recently, the heat capacity of superparamagnetic, non-conducting 13 nm magnetite was measured in our lab (to be published) which had a large value of  $3.46 \text{ mJ} \cdot \text{mol}^{-1} \cdot \text{K}^{-2}$  for the linear term. As an electrical insulator, the linear term in 13 nm magnetite is too large to be associated with the electronic heat capacity, and it is more likely due to its superparamagnetic properties. Likewise, several studies suggest that nanocrystalline hematite is superparamagnetic [12,22,23,63–65] and it is likely that the linear term stems from superparamagnetic effects.

#### 4.7. Effects of uncompensated surface spins

To understand the anomaly found between  $T = (4 \text{ to } 7) \text{ K}$ , the calculated heat capacity from fit-1 was subtracted from the exper-

imentally measured data and the excess heat capacity is shown in figure 8. This anomaly has a sharp rise beginning at  $T = 4 \text{ K}$  and peaking at  $T = 6 \text{ K}$  before slowly declining to a minimum at  $10 \text{ K}$ .

Studies of nanocrystalline hematite using SQUID (superconducting quantum interference device) magnetometry [65] reveal the presence of uncompensated surface spins of  $\text{Fe}^{3+}$  ions. A simple Ising model gives the magnetic entropy per mole of a system as  $S_M = R \ln(2s + 1)$ , where  $s$  is the spin quantum number [25]. If a two-level system is assumed then the entropic contribution per mole of magnetic spin will be  $R \ln 2$ .

The spin concentration can be found by comparing the molar entropy of magnetic spins to the entropic contribution from the anomaly found in the heat capacity of nanocrystalline hematite. The anomaly was fit by hand which data was subsequently fit with an orthogonal polynomial and can be seen by the line in figure 8. The entropy of the magnetic transition was calculated by integrating  $C_{\text{fit}}/T$  over the temperature range (4 to 10) K, and the entropy per mole of  $\text{Fe}_2\text{O}_3 \cdot 0.248\text{H}_2\text{O}$  was found to be  $1.312 \text{ mJ} \cdot \text{mol}^{-1} \cdot \text{K}^{-1}$ . By dividing the entropy of transition by  $R \ln 2$ , the spin concentration was estimated to be  $2.3 \cdot 10^{-4}$  moles spin per mol  $\text{Fe}_2\text{O}_3 \cdot 0.248\text{H}_2\text{O}$ . Another way to interpret this value is that there are only about 2 uncompensated spins for every 10,000  $\text{Fe}_2\text{O}_3$ .

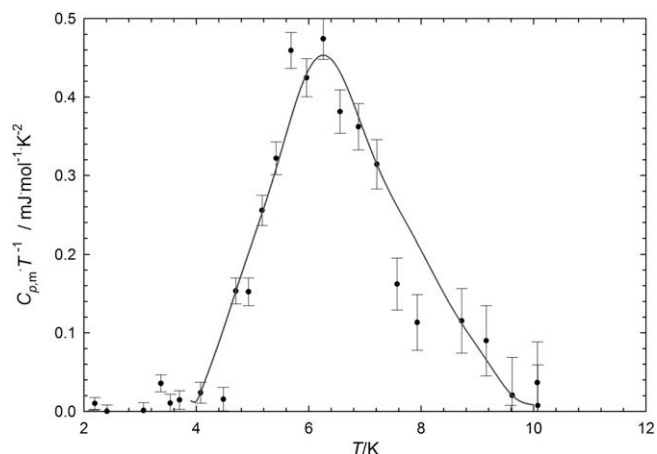


**FIGURE 8.** Plot of  $C_{p,m}/T$  against temperature to show the anomalous heat capacity of 13 nm hematite due to uncompensated surface spins. The vertical bars show the degree of error in each point while the solid line represents an orthogonal fit of the anomaly.



Assuming the unit cell of 13 nm hematite to be similar to that of the bulk [1], there are approximately 648 Fe atoms on the surface of each nanoparticle. From the surface spin calculation, there are only 5.1 spins per nanoparticle meaning that only 0.8% of the surface iron atoms have uncompensated spins. Such a small concentration supports the assumption that the anomaly is likely due to uncompensated surface spins.

#### 4.8. Effects of surface water

Studies by both Navrotsky *et al.* [5] and Boerio-Goates *et al.* [38] have shown that the degree of hydration has a significant effect on the thermodynamic properties of nanoparticles. Since characterization has shown a significant amount of water in this sample and the molar heat capacity of 13 nm hematite is in excess of the bulk hematite, the effects of water on the heat capacity of nanocrystalline hematite should also be considered. In the case of  $\text{TiO}_2$  polymorphs studied by Boerio-Goates *et al.*, it was found that the heat capacity of the bare nanoparticle (contributions of water subtracted) was equal to that of the parent bulk material. By assuming that nanocrystalline hematite will behave in a similar manner, the heat capacity of adsorbed water can be obtained by subtracting contributions equal to bulk hematite from the experimentally measured heat capacity of 13 nm  $\alpha\text{-Fe}_2\text{O}_3 \cdot 0.248\text{H}_2\text{O}$ . Fits of the heat capacity of bulk hematite were obtained from recent measurements [52] in our laboratory. The heat capacity of water adsorbed onto the surface of nanocrystalline hematite was obtained by subtracting that of bulk hematite and dividing the resultant heat capacity by the moles of water (0.248) per mole  $\text{Fe}_2\text{O}_3$ .

The calculated heat capacity of water on the surface of nanocrystalline hematite can be seen in figure 9a. Included in this figure are plots of water on the surface of  $\text{TiO}_2$ , as well as the heat capacity of solid ice [66–69]. In this figure “outer water” on  $\text{TiO}_2$  refers to the heat capacity of samples with the highest degree of hydration:  $\text{TiO}_2 \cdot 0.677\text{H}_2\text{O}$  for anatase and  $\text{TiO}_2 \cdot 0.361\text{H}_2\text{O}$  for rutile. Conversely, “inner water” refers to the removal of significant amounts of adsorbed water on the  $\text{TiO}_2$  polymorphs with samples having the chemical formula  $\text{TiO}_2 \cdot 0.379\text{H}_2\text{O}$  for anatase and  $\text{TiO}_2 \cdot 0.244\text{H}_2\text{O}$  for rutile. To facilitate the comparison between the water on  $\text{TiO}_2$  polymorphs and that on nanocrystalline hematite, a summary of the water contents and surface coverage of these samples can be seen in table 4.

It can be seen that nanocrystalline hematite has a surface coverage similar to that of the inner layer of rutile, yet figure 9b shows that the heat capacity of water on nanocrystalline hematite is higher. This can be explained by hydration enthalpy measurements reported by Navrotsky *et al.* for nanocrystalline  $\text{TiO}_2$  polymorphs [36] and also nanocrystalline hematite [5,35]. These measurements show that as the number of  $\text{H}_2\text{O} \cdot \text{nm}^{-2}$  decreases, the enthalpy of hydration approaches  $150 \text{ kJ} \cdot \text{mol}^{-1}$  for nano- $\text{TiO}_2$  polymorphs while that of nanocrystalline hematite approaches  $100 \text{ kJ} \cdot \text{mol}^{-1}$ . In both cases the nanoparticles hold onto the inner layers of water tenaciously, but  $\text{TiO}_2$  has a higher propensity to hold onto its water. This difference in water binding is manifest in the heat capacity curves shown in figure 9b where the inner water on nano-rutile has a smaller heat capacity than that on nanocrystalline hematite in spite of the similar degrees of hydration.

Further evidence that the heat capacity of surface water decreases with tighter binding is seen when the heat capacity of inner water on anatase is compared to that of rutile. Anatase has both a lower heat capacity and surface coverage (about six  $\text{H}_2\text{O} \cdot \text{nm}^{-2}$  less) than rutile, and according to the measurements of Navrotsky *et al.* the lower surface coverage corresponds to a higher magnitude of hydration enthalpy. In other words the inner water of anatase is bound more tightly than that of rutile because the surface coverage is lower. Overall, these results agree well with

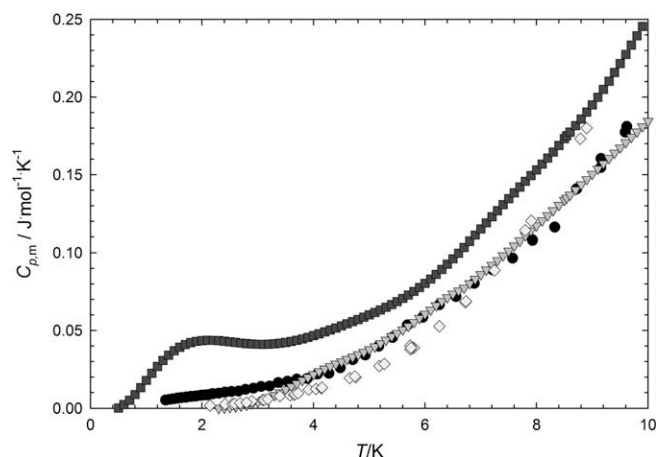


FIGURE 9a. Plot of heat capacity against temperature to show the comparison of the heat capacity of surface  $\text{H}_2\text{O}$  on 13 nm hematite (●) to the outer layers on nanocrystalline rutile (▼) and anatase (■)  $\text{TiO}_2$  [38] as well as hexagonal ice (◇) [69] at temperatures below 10 K.

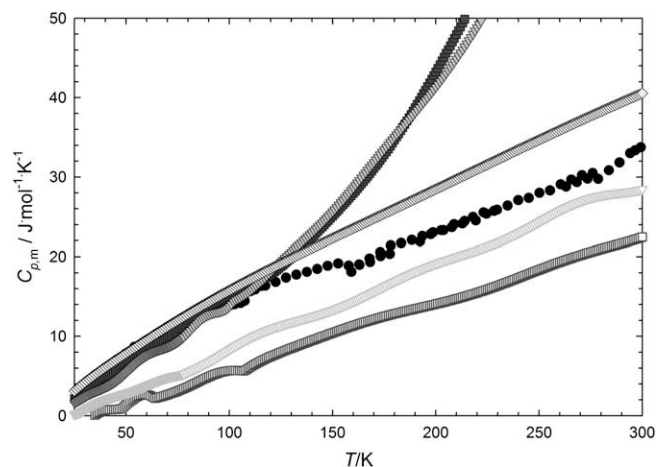


FIGURE 9b. Plot of heat capacity against temperature to show the comparison of the heat capacity of surface  $\text{H}_2\text{O}$  on 13 nm hematite (●) to the outer layers on nanocrystalline rutile (▼) and anatase (■)  $\text{TiO}_2$  [38] as well as hexagonal ice (◇) [66–69]. Open inverted triangles (▽) represent the inner water on rutile while the open squares (□) represent inner water on anatase.

the conclusions of Navrotsky *et al.* and Boerio-Goates *et al.* that the degree of hydration must be taken into account when studying the thermodynamic properties of nanosystems.

A second observation in the heat capacity of the surface water of nanocrystalline hematite is seen in figure 9b where the heat capacity of water on the surface of hematite is higher than that of  $\text{H}_2\text{O(s)}$  below  $T = 7 \text{ K}$ . This is probably less an effect of the water and has more to do with the contributions from uncompensated surfaces spins discussed previously. These magnetic contributions were not part of the bulk hematite heat capacity subtracted from the experimentally measured heat capacity of nanocrystalline hematite, and thus would still be present in the residual heat capacity attributed to water.

#### 4.9. Thermodynamic functions of nanocrystalline hematite

The standard molar thermodynamic functions,  $C_{p,m}^\circ$ ,  $\Delta_0^\circ H_m^\circ$ ,  $\Delta_0^\circ S_m^\circ$ , and  $\Phi_m^\circ = (\Delta_0^\circ S_m^\circ - \Delta_0^\circ H_m^\circ/T)$  scaled by the ideal gas constant  $R$  are reported in table 5 for nanocrystalline hematite ( $\alpha\text{-Fe}_2\text{O}_3 \cdot 0.248\text{H}_2\text{O}$ ). They have been generated at smoothed temperatures



TABLE 5

Standard thermodynamic functions of nanocrystalline hematite ( $\text{Fe}_2\text{O}_3 \cdot 0.248\text{H}_2\text{O}$ ) where  $\Phi_m^\circ = \Delta_0^\circ S_m^\circ - \Delta_0^\circ H_m^\circ/T$ ,  $M = 164.156 \text{ g} \cdot \text{mol}^{-1}$ ,  $p^\circ = 100 \text{ kPa}$ , and  $R = 8.3145 \text{ J} \cdot \text{K}^{-1} \cdot \text{mol}^{-1}$ .

T/K	$C_{p,m}/R$	$\Delta_0^\circ S_m^\circ/R$	$\Delta_0^\circ H_m^\circ/RT$	$\Phi_m^\circ/R$
1.5	0.00022445	0.00019792	0.00010228	0.00079522
2.0	0.00034044	0.00027764	0.00014667	0.0010889
2.5	0.00049156	0.00036910	0.00019988	0.0014070
3.0	0.00068640	0.00047523	0.00026407	0.0017557
3.5	0.00093341	0.00059886	0.00034138	0.0021408
4.0	0.0012408	0.0007429	0.00043392	0.0025687
4.5	0.0016169	0.0009100	0.00054380	0.0030448
5.0	0.0020693	0.0011031	0.00067307	0.0035753
5.5	0.0026059	0.0013248	0.00082372	0.0041662
6.0	0.0032339	0.0015777	0.00099774	0.0048223
6.5	0.0039604	0.0018646	0.0011970	0.0055502
7.0	0.004792	0.002188	0.001424	0.006355
7.5	0.005736	0.002550	0.001679	0.007243
8.0	0.006797	0.002953	0.001965	0.008218
8.5	0.007982	0.003400	0.002283	0.009287
9.0	0.009295	0.003893	0.002636	0.010453
9.5	0.010758	0.004434	0.003024	0.011723
10	0.012321	0.005025	0.003450	0.013102
11	0.015816	0.006359	0.004411	0.016201
12	0.019880	0.007905	0.005526	0.019780
13	0.024606	0.009678	0.006808	0.023868
14	0.030086	0.011698	0.008270	0.028498
15	0.036413	0.013984	0.009930	0.033705
16	0.043678	0.016560	0.011807	0.039518
17	0.05197	0.01945	0.01392	0.04599
18	0.06136	0.02268	0.01629	0.05316
19	0.07195	0.02628	0.01894	0.06105
20	0.08379	0.03026	0.02188	0.06974
25	0.16388	0.056892	0.041665	0.12661
30	0.28210	0.096624	0.071338	0.21024
35	0.43930	0.15142	0.11222	0.32593
40	0.6327	0.2223	0.1648	0.4780
45	0.8569	0.3095	0.2290	0.6693
50	1.1062	0.4125	0.3041	0.9015
55	1.3747	0.5304	0.3891	1.1750
60	1.6581	0.6621	0.4829	1.4894
65	1.9536	0.8064	0.5846	1.8438
70	2.2591	0.9623	0.6933	2.2368
75	2.5732	1.1288	0.8081	2.6667
80	2.8943	1.3051	0.9284	3.1318
85	3.2200	1.4903	1.0536	3.6307
90	3.5478	1.6837	1.1831	4.1623
95	3.8800	1.8839	1.3158	4.7240
100	4.2122	2.0914	1.4523	5.3140
110	4.8756	2.5240	1.7335	6.5730
120	5.5234	2.9761	2.0224	7.9300
130	6.1478	3.4431	2.3160	9.3720
140	6.7477	3.9207	2.6112	10.8880
150	7.324	4.406	2.906	12.471
160	7.879	4.897	3.200	14.108
170	8.414	5.390	3.491	15.793
180	8.928	5.886	3.779	17.521
190	9.422	6.382	4.063	19.283
200	9.894	6.878	4.343	21.075
210	10.342	7.371	4.618	22.893
220	10.768	7.862	4.888	24.730
230	11.171	8.350	5.152	26.586
240	11.554	8.833	5.411	28.455
250	11.918	9.313	5.664	30.334
260	12.267	9.787	5.911	32.221
270	12.601	10.256	6.153	34.114
273.15	12.704	10.403	6.228	34.711
280	12.926	10.720	6.389	36.010
290	13.238	11.179	6.620	37.908
298.15	13.485	11.550	6.804	39.455
300	13.540	11.633	6.846	39.806
310	13.826	12.081	7.066	41.697
320	14.095	12.525	7.282	43.596
330	14.342	12.963	7.492	45.487
340	14.572	13.395	7.697	47.374
350	14.797	13.820	7.897	49.254

TABLE 6

Summary of fits used for calculations of the heat capacity (in  $\text{J} \cdot \text{mol}^{-1} \cdot \text{K}^{-1}$ ) of 13 nm hematite ( $\alpha\text{-Fe}_2\text{O}_3 \cdot 0.248\text{H}_2\text{O}$ ).

Power	Range	Coefficient
	(0.47 to 9.35) K	
1		1.0235E-03
3		9.8187E-05
5		-5.9318E-08
	(9.35 to 94.1) K	
0		-0.052008
1		6.5792E-03
2		1.4609E-03
3		-1.7071E-04
4		1.4695E-05
5		-3.8101E-07
6		4.7122E-09
7		-2.8880E-11
8		7.0689E-14
	(94.1 to 350) K	
0		183.16
1		-8.7099
2		0.17696
3		-1.8567E-03
4		1.1764E-05
5		-4.6340E-08
6		1.1089E-10
7		-1.4751E-13
8		8.3608E-17

The left column lists the power of x, and the right column lists the corresponding coefficient.

by fitting a combination of orthogonal polynomials and fit-1 (given in table 6) to the experimental results for nanocrystalline hematite.

Acknowledgement

This work was financially supported by a grant from the Department of Energy (USA) under Contract Numbered DE-FG02-05ER15666.

References

[1] R.M. Cornell, U. Schwertmann (Eds.), The Iron Oxides: Structure, Properties, Reactions, Occurrence and Uses, VCH, Weinem, 1996.

[2] U. Schwertmann, NATO ASI Ser., Ser. C 217 (1988) 267–308.

[3] A. Manasse, M. Mellini, Eur. J. Mineral. 18 (2006) 845–853.

[4] R.V. Morris, H.V. Lauer Jr., C.A. Lawson, E.K. Gibson Jr., G.A. Nace, C. Stewart, J. Geophys. Res. B 90 (1985) 3126–3144.

[5] A. Navrotsky, L. Mazeina, J. Majzlan, Science (Washington, DC, US) 319 (2008) 1635–1638.

[6] A. Punnoose, K.M. Reddy, A. Thurber, J. Hays, M.H. Engelhard, Nanotechnology 18 (2007). 165502/165501–165502/165506.

[7] U. Schwertmann, R.M. Cornell, Iron Oxides in the Laboratory, second ed., 2000.

[8] S. Morup, C. Frandsen, F. Bodker, S.N. Klausen, K. Lefmann, P.-A. Lindgard, M.F. Hansen, Hyperfine Interact. 144/145 (2003) 347–357.

[9] D. Spagnoli, B. Gilbert, G.A. Waychunas, J.F. Banfield, Geochim. Cosmochim. Acta 73 (2009) 4023–4033.

[10] D.M. Sherman, Geochim. Cosmochim. Acta 69 (2005) 3249–3255.

[11] B. Gilbert, C. Frandsen, E.R. Maxey, D.M. Sherman, Phys. Rev. B: Condens. Matter Mater. Phys. 79 (2009). 035108/035101–035108/035107.

[12] C. Carbone, F. Di Benedetto, C. Sangregorio, P. Marescotti, L.A. Pardi, L. Sorace, J. Phys. Chem. C 112 (2008) 9988–9995.

[13] C.B. de Boer, T.A.T. Mullender, M.J. Dekkers, Geophys. J. Int. 146 (2001) 201–216.

[14] S.H. Gee, Y.K. Hong, J.C. Sur, D.W. Erickson, M.H. Park, F. Jeffers, IEEE Trans. Magn. 40 (2004) 2691–2693.

[15] A.H. Hill, F. Jiao, P.G. Bruce, A. Harrison, W. Kockelmann, C. Ritter, Chem. Mater. 20 (2008) 4891–4899.

[16] C. Cromphaut, V.G. Resende, E. Grave, R.E. Vandenberghe, Hyperfine Interact. 191 (2009) 167–171.

[17] G.F. Goya, M. Veith, R. Rapalaviciute, H. Shen, S. Mathur, Appl. Phys. A: Mater. Sci. Process. 80 (2005) 1523–1526.

- [18] S.N. Klausen, K. Lefmann, P.A. Lindgard, L.T. Kuhn, C.R.H. Bahl, C. Frandsen, S. Moerup, B. Roessli, N. Cavadini, C. Niedermayer, *Phys. Rev. B: Condens. Matter Mater. Phys.* 70 (2004). 214411/214411–214411/214416.
- [19] M.V. Mansilla, R. Zysler, D. Fiorani, L. Suber, *Physica B (Amsterdam, Netherlands)* 320 (2002) 206–209.
- [20] R.D. Zysler, D. Fiorani, A.M. Testa, M. Godinho, E. Agostinelli, L. Suber, *J. Magn. Mater.* 272–276 (2004) 1575–1576.
- [21] R.D. Zysler, D. Fiorani, A.M. Testa, L. Suber, E. Agostinelli, M. Godinho, *Phys. Rev. B: Condens. Matter Mater. Phys.* 68 (2003). 212408/212401–212408/212404.
- [22] T.P. Raming, A.J.A. Winnubst, C.M. van Kats, A.P. Philipse, *J. Colloid Interface Sci.* 249 (2002) 346–350.
- [23] C.R.H. Bahl, The magnetic properties of antiferromagnetic nanoparticles: NiO and  $\alpha$ -Fe<sub>2</sub>O<sub>3</sub>, Information Service Department, Riso National Laboratory, Roskilde, Den., 2006, pp. i–vi, 1–100.
- [24] F. Bodker, M.F. Hansen, C.B. Koch, K. Lefmann, S. Morup, *Phys. Rev. B: Condens. Matter Mater. Phys.* 61 (2000) 6826–6838.
- [25] E.S.R. Gopal, *Specific Heats at Low Temperatures (International Cryogenics Monograph Series)*, Plenum Press, New York, 1966.
- [26] J.B. Ott, J. Boerio-Goates, *Chemical Thermodynamics: Principles and Applications*, Academic Press, California, 2000.
- [27] O. Bomati-Miguel, L. Mazeina, A. Navrotsky, S. Veintemillas-Verdaguer, *Chem. Mater.* 20 (2008) 591–598.
- [28] J. Majzlan, K.-D. Grevel, A. Navrotsky, *Am. Mineral.* 88 (2003) 855–859.
- [29] J. Majzlan, C.B. Koch, A. Navrotsky, *Clays Clay Miner.* 56 (2008) 526–530.
- [30] J. Majzlan, B.E. Lang, R. Stevens, A. Navrotsky, B.F. Woodfield, J. Boerio-Goates, *Am. Mineral.* 88 (2003) 846–854.
- [31] J. Majzlan, L. Mazeina, A. Navrotsky, *Geochim. Cosmochim. Acta* 71 (2007) 615–623.
- [32] J. Majzlan, A. Navrotsky, U. Schwertmann, *Geochim. Cosmochim. Acta* 68 (2004) 1049–1059.
- [33] J. Majzlan, A. Navrotsky, B.F. Woodfield, B.E. Lang, J. Boerio-Goates, R.A. Fisher, *J. Low Temp. Phys.* 130 (2003) 69–76.
- [34] L. Mazeina, A. Navrotsky, *Clays Clay Miner.* 53 (2005) 113–122.
- [35] L. Mazeina, A. Navrotsky, *Chem. Mater.* 19 (2007) 825–833.
- [36] A. Navrotsky, *J. Chem. Thermodyn.* 39 (2006) 2–9.
- [37] N.E. Phillips, *Crit. Rev. Solid State Sci.* 2 (1971) 467–553.
- [38] J. Boerio-Goates, G. Li, L. Li, T.F. Walker, T. Parry, B.F. Woodfield, *NanoLetters* 6 (2006) 750–754.
- [39] G.S. Parks, K.K. Kelley, *J. Phys. Chem.* 30 (1926) 47–55.
- [40] F. Grønqvold, E.F. Westrum Jr., *J. Am. Chem. Soc.* 81 (1959) 1780–1783.
- [41] K.D. Jayasuriya, A.M. Stewart, S.J. Campbell, *J. Phys. Chem. Solids* 46 (1985) 625–629.
- [42] V.V. Korolev, I.M. Arefyev, A.V. Blinov, *J. Therm. Anal. Calorim.* 92 (2008) 697–700.
- [43] Y. Volokitin, J. Sinzig, L.J. de Jongh, G. Schmid, M.N. Vargaftik, I.I. Moiseev, *Nature (London)* 384 (1996) 621–623.
- [44] Y.Y. Chen, Y.D. Yao, S.S. Hsiao, S.U. Jen, B.T. Lin, H.M. Lin, C.Y. Tung, *Phys. Rev. B: Condens. Matter* 52 (1995) 9364–9369.
- [45] N.X. Sun, K. Lu, *Phys. Rev. B: Condens. Matter* 54 (1996) 6058–6061.
- [46] T.H.K. Barron, W.T. Berg, J.A. Morrison, *Proc. R. Soc. Lond., Ser. A* 250 (1959) 70–83.
- [47] C.D. Terwilliger, Y.-M. Chiang, *J. Am. Ceram. Soc.* 78 (1995) 2045–2055.
- [48] H. Zhang, J.F. Banfield, *Nanostruct. Mater.* 10 (1998) 185–194.
- [49] S. Liu, Q. Liu, J. Boerio-Goates, B.F. Woodfield, *J. Adv. Mater. (Covina, CA, US)* 39 (2007) 18–23.
- [50] R. Stevens, J. Boerio-Goates, *J. Chem. Thermodyn.* 36 (2004) 857–863.
- [51] J.C. Lashley, B.E. Lang, J. Boerio-Goates, B.F. Woodfield, T.W. Darling, F. Chu, A. Migliori, D. Thoma, *J. Chem. Thermodyn.* 34 (2002) 251–261.
- [52] C.L. Snow, Q. Shi, J. Boerio-Goates, B.F. Woodfield, *J. Chem. Thermodyn.* (accepted for publication).
- [53] R.A. Fisher, F. Bouquet, N.E. Phillips, J.P. Franck, G. Zhang, J.E. Gordon, C. Marcenat, *Phys. Rev. B: Condens. Matter Mater. Phys.* 64 (2001). 134425/134421–134425/134429.
- [54] J. Boerio-Goates, R. Stevens, B. Lang, B.F. Woodfield, *J. Therm. Anal. Calorim.* 69 (2002) 773–783.
- [55] J.M.D. Coey, S. Von Molnar, A. Torressen, *J. Less-Common Met.* 151 (1989) 191–194.
- [56] P.E. Joensson, *Adv. Chem. Phys.* 128 (2003) 191–248.
- [57] J.D. Livingston, C.P. Bean, *J. Appl. Phys.* 32 (1961) 1964–1966.
- [58] C.P. Bean, J.D. Livingston, *J. Appl. Phys.* 30 (1959) 1205–1295.
- [59] B.B. Triplett, N.E. Phillips, *Phys. Lett. A* 37 (1971) 443–444.
- [60] C.L. Snow, Q. Shi, S.J. Smith, B.E. Lang, L. Mazeina, A. Navrotsky, J. Boerio-Goates, B.F. Woodfield, *J. Chem. Thermodyn.* (2010), (submitted for publication).
- [61] B.W. Veal, J.A. Rayne, *Phys. Rev.* 128 (1962) 551–555.
- [62] D. Chakrabarti, *Transport properties of chromium–aluminum solid solution alloys*, Dissertation, University of Illinois-Urbana, Microfilms No. 71-5066, Ann Arbor, MI, 1970.
- [63] F. Bodker, S. Morup, *Europhys. Lett.* 52 (2000) 217–223.
- [64] H. Fan, B. Song, Z. Yang, Q. Li, *Nanotechnology* 16 (2005) 1100–1104.
- [65] V. Zelenak, A. Zelenakova, J. Kovac, U. Vainio, N. Murafa, *J. Phys. Chem. C* 113 (2009) 13045–13050.
- [66] P. Flubacher, A.J. Leadbetter, J.A. Morrison, *J. Chem. Phys.* 33 (1960) 1751–1755.
- [67] W.F. Giauque, J.W. Stout, *J. Am. Chem. Soc.* 58 (1936) 1144–1150.
- [68] O. Haida, T. Matsuo, H. Suga, S. Seki, *J. Chem. Thermodyn.* 6 (1974) 815–825.
- [69] S.J. Smith, B.E. Lang, S. Liu, J. Boerio-Goates, B.F. Woodfield, *J. Chem. Thermodyn.* 39 (2007) 712–716.